

Hercules X-1: Empirical Models of UV Emission Lines

Bram Boroson and Timothy Kallman

Goddard Space Flight Center, Greenbelt, MD 20771; bboroson@falafel.gsfc.nasa.gov,
tim@xstar.gsfc.nasa.gov

and

Saeqa Dil Vrtilek and John Raymond

Harvard-Smithsonian Center for Astrophysics; svrtilek@cfa.harvard.edu,
jraymond@cfa.harvard.edu

and

Martin Still and Manuel Bautista

Goddard Space Flight Center, Greenbelt, MD 20771; still@chunky.gsfc.nasa.gov,
bautista@gsfc.nasa.gov

and

Hannah Quaintrell

The Open University, Walton Hall, Milton Keynes MK7 6AA, UK

ABSTRACT

The UV emission lines of Hercules X-1, resolved with the HST GHRS and STIS, can be divided into broad ($\text{FWHM} \approx 750 \text{ km s}^{-1}$) and narrow ($\text{FWHM} \approx 150 \text{ km s}^{-1}$) components. The broad lines can be unambiguously identified with emission from an accretion disk which rotates prograde with the orbit. The narrow lines, previously identified with the X-ray illuminated atmosphere of the companion star, are blueshifted at both $\phi = 0.2$ and $\phi = 0.8$ and the line flux at $\phi = 0.2$ is ≈ 0.2 of the flux at $\phi = 0.8$. Line ratio diagnostics show that the density of the narrow line region is $\log n_e = 13.4 \pm 0.2$ and $T_e = 1.0 \pm 0.2 \times 10^5 \text{ K}$. The symmetry of the eclipse ingress suggests that the line emission on the surface of the disk is left-right symmetric relative to the orbit. Model fits to the O V, Si IV, and He II line profiles agree with this result, but fits to the N V lines suggest that the receding side of the disk is brighter. We note that there are narrow absorption components in the N V lines with blueshifts of $\approx 500 \text{ km s}^{-1}$.

1. Introduction

The transfer of matter from the donor star to the compact object in an X-ray binary has proved to be unexpectedly difficult to understand. At first it would appear that the problem is governed simply by classical hydrodynamics and the boundary conditions are set by the masses and separation of the two stars. (The latter quantities are well known in the case of eclipsing pulsars.) The gross structure of accretion disks and mass transfer has indeed been described by theory (Shakura & Sunyaev 1973; Lubow & Shu 1975). However, difficulties are presented by observations of unexpected behavior, by the realization that X-ray heating is important even in the presence of strong viscous heating in the disk interior (Dubus et al. 1999) and that instabilities from the effects of the radiation on the dynamics may play an important role (Pringle 1996). Important physical processes in accretion disks, such as the viscous transport of angular momentum, the generation of magnetic fields, the nature of disk coronae and winds (Begelman & McKee 1983; Begelman, McKee, & Shields, 1983), and turbulence within the disk and in the interaction with the gas stream from the companion (Armitage & Livio 1998), have been characterized or parameterized, but our understanding is still in an exploratory stage and has not been confirmed by observation.

Several X-ray binaries, including Her X-1, SS 433, LMC X-4, GX 354-0, and Cyg X-2, vary on time scales of months (Levine et al. 1996, Kong et al. 1998). Cataclysmic variables such as TV Col, V603 Aql, and TT Ari also show periods longer than their orbits (Schwarzenberg-Czerny 1992). These variations are usually attributed to a precession of the accretion disk which periodically blocks our line of sight to the central X-ray source. Although the analogy between the disk motion and solid-body precession is not accurate (Kondo, Wolff, & van Flandern 1983), we will use the conventional term “precession” for the disk wobble. For the non-eclipsing systems GX 354-0 and Cyg X-2, the modulation is gradual and never leads to total obscuration. This suggests that either the occulting region is on the order of the same size as the emitting region or that the X-rays are attenuated by an optically thin absorber (for example, a disk corona). Jets precess with the X-ray period in SS 433, and the X-ray pulse profiles vary with the long-term period in Her X-1. These phenomena suggest that any precession or warping includes the outer accretion disk and extends far into the inner disk.

There have been many attempts to explain the long-term period in Hercules X-1, the first X-ray source to have a “superorbital” period identified. Most recently, following work of Iping & Petterson (1990), Pringle (1996) showed that warped accretion disks are unstable to the re-radiation pressure that follows from the non-axisymmetric X-ray illumination by the central source. This theory has been applied to warped disks in Active Galactic Nuclei, X-ray binaries, T Tauri stars, and disks about Young Stellar Objects (Maloney, Begelman,

& Pringle 1996). According to the model, the warp should extend to the inner edge of the disk (where the disk may even flip over, Pringle 1997). Radiation-driven warping has the advantage of predicting a global disturbance in the disk, in which precession occurs at a single period at various radii within the disk. The periods predicted are of the same order of magnitude as observed periods; however, it is impossible for the theory to explain the variations among individual sources, as the period depends on imprecisely known parameters such as the disk viscosity and accretion efficiency.

Axisymmetric disks and their vertical structure have been investigated theoretically (Shakura & Sunyaev 1973), and the spectra of the X-rays reprocessed by the surface have been computed (Vrtilek et al. 1990, Raymond 1993, Ko & Kallman 1994, van Paradijs & McClintock 1995). While there is abundant evidence that disks do reprocess X-rays into optical and UV line and continuum emission, the reprocessing scenarios involving an axisymmetric disk require that the disk be flared in order for the outer disk to have an unobstructed view of the central X-ray source. However, the standard demonstration that disks should be flared assumes an isothermal vertical structure for the disk; without this unrealistic assumption, disks would be convex (Dubus et al. 1999).

Ultraviolet wavelengths are ideal for investigating reprocessing in X-ray binaries as they contain strong resonance lines from ions that are sensitive to X-ray illumination. Hercules X-1 is a prime target for study in the UV, as it is fortuitously far from the Galactic plane (≈ 3 kpc), so that its interstellar reddening is low ($E(B - V) < 0.05$). Observations with IUE (Dupree et al. 1978, Gursky et al. 1980, Howarth & Wilson 1983; Boyle et al. 1986; Vrtilek, Cheng, & Raymond 1996) and the Faint Object Spectrograph (FOS) aboard HST (Anderson et al. 1994) show that the resonance emission lines of N V $\lambda\lambda$ 1238.8, 1242.8 and C IV $\lambda\lambda$ 1548, 1550 are much stronger than the most prominent optical emission lines, He II λ 4686 and the Bowen blend at 4640 Å (Still et al. 1997). Boroson et al. (1996) used the Goddard High Resolution Spectrograph (GHRS) aboard HST to resolve the N V lines into broad and narrow components, which they attributed to the accretion disk and the X-ray illuminated atmosphere of the companion star, respectively. There was no evidence for double-peaked profiles typical of accretion disks, and the doublet ratios suggested conditions intermediate between optically thick and thin limits. Both double-peaked profiles and optically thick conditions had been expected on theoretical grounds (Raymond 1993, Ko & Kallman 1994). UV observations of Sco X-1 (Kallman, Boroson, & Vrtilek 1998) also show profiles that are not double-peaked and doublet ratios indicating intermediate optical depth.

Considering the uncertainties in current theory and the wealth of observational details that have yet to find a satisfactory explanation, we undertake here an *empirical* study of the

kinematics of accretion in Hercules X-1, based primarily on the UV line profiles observed recently with the Space Telescope Imaging Spectrograph (STIS) aboard the Hubble Space Telescope (HST). These data were part of a multiwavelength campaign (Vrtilek et al. 1999) that included simultaneous X-ray observations with the Rossi X-ray Timing Explorer (RXTE), the Extreme Ultraviolet Explorer (EUVE), and ground-based optical telescopes. Simultaneous BeppoSAX observations were obtained independently of our multiwavelength campaign. Further multiwavelength observations of Her X-1 are scheduled for July 1999 and should provide further tests of the models presented here.

2. Observations

The observations took place during the “short-on” phase of the 35-day cycle of Her X-1 (Jones, Forman, & Liller 1973). Introducing the long-term phase $\Psi = 0.0$ at X-ray turn-on, the short-on stage occurs during $\Psi = 0.55 - 0.75$ (Scott & Leahy 1999). Using the last turn-on recorded by the RXTE All Sky Monitor and reported by Scott & Leahy (2 cycles before the start of our observation) and applying a long-term period of 34.853 days. This period is exactly 20.5 times the binary period, in agreement with epoch folding of the ASM data and the observation that 35-day turn-ons occur at $\phi = 0.2$ or $\phi = 0.7$ with equal frequency (Scott & Leahy). With this long-term period and ephemeris, we find that the UV observations spanned $\Psi = 0.64$ through $\Psi = 0.74$.

The UV observations used the Space Telescope Imaging Spectrograph (STIS) aboard the Hubble Space Telescope (HST). The STIS instrument design is described by Woodgate et al. (1998), and the in-orbit performance of the STIS is described by Kimble et al. (1998). The STIS Multianode Microchannel Array (MAMA) detectors were more sensitive to passage of the satellite through the South Atlantic Anomaly than expected, so that we could only observe Hercules X-1 during those HST orbits that did not intersect the SAA. We thus had to observe in a pattern of 5 HST orbits followed by 10 HST orbits without observations. Furthermore, 5 of our HST orbits produced no data due to a hardware problem. This paper discusses the results of the 15 successful HST orbits in July of 1998 (each orbit provided ≈ 45 minutes of data). Light curves of the UV flux observed with the STIS compared with light curves in the X-ray, EUV, and optical, are shown in Vrtilek et al (1999).

A log of the STIS observations is shown in Table 1. For observations extending into mid-eclipse we used the G140L grating, appropriate for first-order spectroscopy with resolution $R = \lambda/2\Delta\lambda = 960 - 1440$ ($200 - 300 \text{ km s}^{-1}$) in the wavelength range $1150 - 1720\text{\AA}$. For these observations we used the ACCUM mode to accumulate spectra in

time intervals of 185 seconds.

For the other 10 HST orbits, we used the E140M grating for high resolution echelle spectroscopy. This provides spectral coverages of, $1150 - 1710\text{\AA}$ with a resolving power of $R = 45,800$ (6 km s^{-1}). For these exposures, we used the TIME-TAG mode on the STIS, which stamps each photon detected with a time accurate to $125 \mu\text{sec}$. We show the average spectrum for $\phi = 0.685$ through $\phi = 0.764$ in Figure 1, and identify emission lines. There are also many interstellar absorption features in the spectrum which we will discuss in a later paper (Borosen et al. 1999).

3. Gaussian Fits

Before interpreting the spectra, we fit the lines with a sum of two Gaussians, one broad and one narrow. In fitting two components, our motivation is to test the interpretation of Borosen et al. (1996) that there are two emission regions and that the broad component arises in the disk and the narrow component on HZ Her. Although there is no compelling reason for the lines to have Gaussian shapes, the fits will allow us to obtain approximate line strengths, doublet ratios, and Doppler shifts over the course of the orbit. As the doublet components and separate line components overlap, a fit to estimate their separate contributions is needed.

We added together echelle orders where they overlapped, weighting the fluxes by the inverse square of the errors, and adding weighted errors in quadrature. To fit doublets, we assumed each doublet component has the same Doppler shift relative to its rest wavelength, and allow a doublet ratio as a free parameter.

For some lines and some orbital phases, the signal to noise ratio in the lines only warranted a fit with a single Gaussian. We also fit a flat continuum; when we did not obtain adequate fits, we allowed a linear continuum. We determined errors in our fitted parameters using a bootstrap method (Press et al. 1992). Orbital phases at each exposure were determined using the ephemeris of Deeter et al. (1991).

Examples of the fits to the N V $\lambda\lambda$ 1238.8, 1242.8, O V λ 1371, Si IV λ 1393, He II λ 1640, and C IV $\lambda\lambda$ 1548, 1550 lines are shown in Figures 2 through 6, respectively. For the Si IV λ 1393 and C IV $\lambda\lambda$ 1548, 1550 lines, we allow free parameters corresponding to the optical depth and velocity width of an interstellar absorption line at -60 km s^{-1} heliocentric velocity. The best fit parameters and χ^2 values for all lines are shown in Table 2. In Table 3 we list the doublet ratios of the N V broad and narrow components as a function of orbital phase. In Figure 7 we show the orbital variation in line velocity, and in Figure 8 we show

the orbital variation in line flux for the N V line.

We list the lines at $\phi = 0.057$ under “broad lines” for reasons that will become clear in §4 and §5.

4. Basic Interpretation

There are four compelling reasons to identify the broad line region with the accretion disk about the neutron star, as was done by Boroson et al. (1996). First, the width of the lines (average FWHM= 750 km s⁻¹) is most naturally explained as the result of Keplerian broadening in a disk with radius $r \approx 1 - 2 \times 10^{11}$ cm, where the velocity at the disk edge would be $(GM/r)^{1/2} \sin i \approx 300 - 400$ km s⁻¹. Models predict accretion disk emission lines should be double-peaked, with the peaks at \pm the projected velocity at the edge of the disk (Smak 1981). The FWHM of such a profile should thus be about twice the velocity at the disk edge, or $\approx 600 - 800$ km s⁻¹.

Second, the behavior of the broad lines at phases $\phi = \pm 0.1$ is consistent with that expected when HZ Her partially occults a Keplerian disk. The lines at $\phi = 0.057$ are blue-shifted, as expected if the disk rotates prograde with the binary orbit, so that the approaching side of the disk emerges first from eclipse. The magnitude of the Doppler shift, 400 km s⁻¹, rules out the companion star as the source of this emission. This explanation is consistent with the line profiles observed with the GHRS at $\phi = 0.88$ and $\phi = 0.91$; the approaching side of the disk is also the first to enter eclipse.

A third reason to identify the broad lines with the disk is the variation of line flux with orbital phase (Figure 8). The broad lines are roughly constant in flux from $\phi = 0.1$ to 0.2 and from $\phi = 0.65$ through $\phi = 0.8$. The STIS low-resolution spectra from $\phi = 0.90 - 0.98$ show a steadily decreasing flux in the lines, consistent with the progressive occultation of a spatially extended region about the neutron star.

Finally, evidence that is somewhat less compelling is provided by the Doppler shifts of the broad lines over the course of the orbit (Figure 7). As observed previously with the GHRS, the broad N V lines are redshifted at $\phi \approx 0.75$ at ≈ 200 km s⁻¹(heliocentric), consistent with the neutron star orbital velocity of 169 km s⁻¹. At $\phi \lesssim 0.2$, the broad N V lines have shifted towards the blue, to ≈ 0 km s⁻¹heliocentric velocity. Although this is not as much expected from the orbital motion of the neutron star, we note that the other lines (Si IV, He II, C IV) are further blueshifted (Figure 7). The O V $\lambda 1371$ line appears to have either an absorption component or a separate narrow emission component which renders our line fits uncertain at phases $\phi < 0.211$. We suspect that scattered emission (to be

discussed in Boroson et al. 1999) may be affecting the fits. We also note that at $\phi = 0.211$, there appears to be emission towards the blue that is in excess of the Gaussian fit to the N V line.

We identify the narrow line region with the X-ray heated atmosphere of HZ Her, as we did in Boroson et al. (1996). Our principal reason for this identification (following Boyle et al. 1986) is that the orbital phase dependence of the line flux resembles the phase dependence of the UV continuum (Figure 9), most of which is assumed to arise in the X-ray heated face of the companion star. The flux increases from $\phi = 0.1$ to $\phi = 0.4$ and decreases from $\phi = 0.6$ to $\phi = 0.9$ as the projected area of the X-ray heated atmosphere increases and then decreases, but between $\phi = 0.4$ and $\phi = 0.6$ there is a plateau or secondary minimum as the accretion disk occults the star. The total flux should be the total of the flux from the disk and the flux from HZ Her, and the former should be roughly constant over the orbit outside of eclipse. Difficulties with this picture are highlighted in §8.

5. Eclipse Maps and Broad Line Fits

5.1. Low-resolution maps of line flux

The eclipse ingress, observed with the STIS in low-resolution mode, can be used as a direct test of the left-right asymmetry (relative to the orbital plane) of the emission in the disk. This can be a useful test of the hypothesis that the disk is warped, although if the line emission is in response to X-rays scattered by a corona, a warped disk can still produce line emission that is axisymmetric on its surface.

Given masses and separations of the two stars, we can find at a given orbital phase ϕ the distance x from the center of the accretion disk beyond which the disk is occulted by the surface of the star. We assume that the eclipsing edge of HZ Her is flat relative to our view of the accretion disk. We have tested this simplifying assumption by using a model similar to that of Howarth & Wilson (1983a) to find the actual shape of the eclipsing edge. We find that the actual eclipse edge has an rms deviation from a straight line of $\lesssim 5\%$ of the radius of the outer edge of the disk.

If the disk is symmetric, then we expect that

$$F_{\text{disk}} - F(x) = F(-x) \tag{1}$$

That is, the amount of flux occulted when the shadow line passes within x of the neutron star is the same as the amount remaining when the shadow line has passed the same distance to the other side of the neutron star.

This suggests that if we were to plot $(x, F_{\text{disk}} - F(x[\phi]))$ and $(-x[\phi], F(-x[\phi]))$ that they would overlap, given axisymmetric emission on the disk. We show the results of this test in Figure 10, for the continuum flux, for the flux in the N V lines, and for the flux in the C IV lines. The results are consistent with a disk that has left-right symmetry. The asymmetry in the C IV lines can be attributed to the interstellar absorption lines observed with the STIS in echelle mode. The absorption component at 1548Å is stronger than the component at 1550Å, so that we expect to observe less flux from C IV when the broad line is blue-shifted, and more of the 1550Å line overlaps the 1548Å interstellar absorption line. The emission remaining after the disk has started to become eclipsed becomes progressively more blue-shifted, so that more of the 1550Å emission line overlaps with the 1548Å interstellar absorption line.

5.2. Fits to line profiles

We also fit the line profiles at $\phi = 0.057, 0.092$, and 0.132 , phases during the eclipse egress when the narrow line is not prominent. An axisymmetric distribution of emission leads to a double-peaked profile, which does not fit the observation. We assume instead that the surface brightness of the disk at radius r and angle θ is given by

$$F(r, \theta) = r^\alpha B(\theta) \quad (2)$$

where α is a free parameter. We have set as free parameters $B(\theta)$ at 3 equally spaced values of θ from 0 to π (that is, in 60° intervals; we force the disk to have front-back symmetry, as the eclipse progression does not allow us to distinguish between front and back of the disk.) We linearly interpolate $B(\theta)$ for values of θ between each of the 3 fixed points. We allow the emission from a point in the disk to be spread into a Gaussian with velocity width Δv . The doublet ratio and Δv are both free parameters. Whether a point on the disk contributes emission at a given ϕ depends on its position relative to the eclipse line. We fix $M \sin i$ to be $1.4 M_\odot$. We transform the velocities of our computed profiles to account for the neutron star’s orbit about the center of mass using $v' = v - (169 \text{ km s}^{-1}) \sin 2\pi\phi$.

We show the results of fits to the N V $\lambda\lambda 1238.8, 1242.8$ doublet in Figure 11. The best-fit value of $\alpha = -1.5$, the best-fit disk radius is 1.8×10^{11} cm, the doublet ratio 1.46, the turbulent velocity $\Delta v = 130 \text{ km s}^{-1}$, and the emissivity versus angle on the disk is $B(\theta) = (6.6, 5.8, 1.0)$ for $\theta = (0, \pi/2, \pi)$. If we exclude from the fit regions near the narrow absorption lines at -500 km s^{-1} (see §7), we still find that the red-shifted side of the disk is brighter: $B(\theta) = (3.0, 1.2, 1.0)$.

The other lines show different best-fit angular brightness profiles, although the counting

statistics are not as good for these lines as for N V $\lambda\lambda$ 1238.8, 1242.8 . The Si IV λ 1394 line is fit with similar parameters as the N V line, but $B(\theta) = (1.7, 0.5, 1.0)$. For He II, we find $B(\theta) = (1.9, 1.9, 1.0)$, and for O V λ 1371, we find $B(\theta) = (1.2, 0.64, 1.0)$. The best-fit outer radius for the disk from the O V profile is 10^{11} cm. It is reasonable to expect that O V λ 1371 is emitted at smaller radii in the disk than the other lines, as it is preferentially emitted at high densities. The low-resolution spectra during eclipse ingress show that O V emission disappears at $\phi = 0.95$, while the other emission lines are present. At this orbital phase, only regions further than 7×10^{10} cm from the neutron star are visible.

We also compare the predictions of the best-fit model for the N V lines with the broad lines seen at $\phi = 0.88$ and $\phi = 0.91$ with the GHRS (Boroson et al. 1996). To fit the GHRS lines, we fix the parameters determined by the fits to the STIS spectra, except for the normalization of the line flux, and allow all velocities to be multiplied by some factor. We find the χ^2 deviation from the data is minimized when the fluxes are multiplied by 1.5 and the velocities are multiplied by 0.94.

6. Density and Temperature Diagnostics

There are several lines (principally due to O and S) in the UV spectrum observed with STIS that can be used to examine the density and temperature of the emitting gas. To aid our analysis of the line ratios, we use the atomic data of the development version of XSTAR, a photoionization code based on Kallman & McCray (1982).

As suggested by previous observers (e.g. Howarth & Wilson 1983b), the Si IV λ 1403 line is blended with a complex of O IV lines. With the echelle mode of the HST STIS, we can now resolve the separate lines of this blend. These lines have been used previously in solar astronomy (Cook et al. 1995) as a density diagnostic. Nearby S IV lines at 1423.8 and 1416.9Å lines also provide a density diagnostic (Dufton et al. 1982).

In Figure 12 we show the average STIS spectra between $\lambda = 1390$ and $\lambda = 1430$ for $\phi = 0.65$ through $\phi = 0.80$. This is the phase range in which the narrow lines are most prominent; because the wavelength separation of the lines is $\sim 400\text{km s}^{-1}$, we are not able to separate them at phases when only the broad components are visible. Narrow lines are also easier to detect against a noisy background than broad lines. The O IV lines at 1338, 1343Å are, surprisingly, about twice as broad as the narrow N V components, but the line flux varies over orbital phase in a manner similar to the narrow lines. Thus the line ratios we form should allow us to infer physical conditions in the narrow line region only.

We estimate the errors in our measurement of the flux in the lines solely from the

counting statistics. Realistically, errors are also introduced by our choice of continuum, but these are difficult to characterize.

We can also form a density diagnostic from the ratio of O V λ 1371 and O V λ 1218. Although O V λ 1218 is diminished by the saturated Ly α interstellar absorption line, we correct for this by fitting the absorption profile to a Lorentzian. We first adjust the continuum level so that the saturated flux does not go below 0, to correct for a possible systematic error in the background subtraction. We then find an interstellar column density of $N_{\text{H}} = 1.0 \pm 0.1 \times 10^{20} \text{ cm}^{-2}$. This is within a factor of 2 of values derived from the X-ray absorption (Vrtilek & Halpern 1985 found $N_{\text{H}} = 4.6 \times 10^{19} \text{ cm}^{-2}$ absorbing the blackbody flux seen with Einstein; Mavromatakis 1993 found $N_{\text{H}} = 1.1 \pm_{-0.7}^{0.4} \times 10^{20} \text{ cm}^{-2}$ with ROSAT, and Dal Fiume et al. 1998 found $N_{\text{H}} = 5.1 \pm 0.07 \times 10^{19} \text{ cm}^{-2}$ with BeppoSAX.) For standard relations between E(B-V) and N_{H} (Bohlin 1975), we find E(B-V) = 0.018 ± 0.002 . From the model of the interstellar Ly α line, we find we must adjust the observed flux in the O V λ 1218 line by a factor of 2.

We obtain the following values for the density diagnostic line ratios:
 S IV λ 1423/1417 = 0.9 ± 0.3 , O IV λ 1407/1401 = 0.6 ± 0.2 , O IV λ 1407/1339 = 0.6 ± 0.2 ,
 O IV λ 1401/1343 = 0.9 ± 0.3 , O IV λ 1407/1343 = 0.5 ± 0.2 , O V λ 1218/1371 = 0.42 ± 0.07 ,
 and S V λ 1199/1502 > 6. (The S V λ 1199 line overlaps interstellar N I absorption).

In Figure 13 we show the densities and temperatures implied by these line ratios. The best agreement for the various line ratios is found at $\log n_e = 13.4 \pm 0.2$, $T_e = 1.0 \pm 0.2 \times 10^5 \text{ K}$. We note that the S IV ratio is not very sensitive to the temperature (for a 1σ change in the ratio, $T_e = 4 \times 10^5 \text{ K}$ is consistent with a density of $\log n_e = 12.5$.) However, the S IV ratio can rule out $T_e > 6 \times 10^5 \text{ K}$, and we do not expect temperatures $T_e > 2 \times 10^5 \text{ K}$ in any case, as even in coronal ionization balance, the fraction of O IV ions should be negligible. The S V ratio predicts lower temperatures than the other ratios. Even lower temperatures would be predicted if, as we suspect, the flux in the λ 1199 line is diminished by interstellar N I absorption. Recombination from S VI may make a small contribution to the S V emission, however, bringing the temperatures into agreement with those predicted by the O IV and O V ratios. Our results for the density are similar to those of Howarth & Wilson (1983b), who found $\log n_e = 13.3$ and $T = 2.5 \times 10^4 \text{ K}$. The temperature they found does not appear to be consistent with the O IV ratios, although it does agree with the S V ratio.

From the measured flux in the O IV, O V, and S IV, S V lines, the measured density, and from the emissivities of the ions at the measured temperature, we can estimate the emitting volume. We assume that all O is in either O IV or O V stages, and that all S is in either S IV or S V. From the line ratio S IV λ 1424/S V λ 1502 we find $N(\text{S IV})/N(\text{S V}) = 18 \pm 4$ (the value in collisional ionization balance should be 900). From O IV λ 1338/O V λ 1218

we find $N(\text{O IV})/N(\text{O V}) = 1.7 \pm 0.5$ (the value for collisional ionization is 240). This is further evidence that the gas is in photoionization equilibrium at $T \lesssim 10^5$ K. Assuming a distance to Her X-1 of 5.5 kpc, both the O and S lines imply $V \approx 10^{24}$ cm³. Such a volume of emitting gas is easy to accommodate within the system.

Observations with the Hopkins Ultraviolet Telescope (Boroson et al. 1997) during orbital phases when the narrow lines are prominent show that the flux in the O VI $\lambda\lambda 1032, 1038$ lines is approximately equal to that in the N V $\lambda\lambda 1238.8, 1242.8$ lines. Using the volume inferred from the O lines, the O VI doublet flux inferred from the N V $\lambda\lambda 1238.8, 1242.8$ doublet, and the O VI emissivity, we find that $\approx 8 \times 10^{-3}$ of the O is in O VI. This supports our assumption that all O is in O IV or O V.

7. Absorption Lines

The N V lines show narrow absorption features at blueshifts of 500 km s^{-1} , with velocity widths of $b \approx 50 \text{ km s}^{-1}$ (Figure 14) and equivalent widths $W_\lambda \approx 0.1 \text{ \AA}$. There is also evidence for absorption lines at -500 km s^{-1} in C IV $\lambda 1548.195$ ($W_\lambda \sim 0.2 \text{ \AA}$, only seen at $\phi = 0.057$).

It is unlikely that these features are artifacts, because they persist for several HST orbits and are separated by exactly the doublet separation in N V. The lines are probably not interstellar. The right-hand panel of Figure 14 shows that as the flux increases as Her X-1 emerges from eclipse, the lines do not become significantly stronger, as they would if a constant optical depth were applied to the changing flux.

This suggests that the absorbing gas may only be in front of the emitting region which is visible at $\phi = 0.057$. For example, a region above the front of the disk could absorb emission from the back of the disk. The problem with the scenario linking the absorption lines to a region of the disk is that the neutron star line-of-sight velocity, and thus velocities on the accretion disk, should vary by $\approx 100 \text{ km s}^{-1}$ from $\phi = 0.057$ to $\phi = 0.171$, and yet the absorption feature remains stationary.

8. Discussion

One surprising result of the analysis of the eclipse ingress is that the disk appears to be roughly left-right symmetric in its continuum and N V emission. The analysis that leads to this conclusion, however, depends on our knowledge of the position of the eclipsing limb of HZ Her, that the disk is only occulted by this limb and not by, for example, the gas stream,

on our assumed value for the total flux of the disk, that the disk emission is constant over the course of the ingress, and that there is no other variable source of line or continuum emission during the eclipse ingress. It would be more satisfying to compare the flux at say $\phi = 0.94$ during one eclipse ingress with the flux at $\phi = 0.06$ during the eclipse egress immediately following.

The disk line profiles are not generally double-peaked. We can fit the profiles if we make the empirical assumption that the emission varies with angle on the disk surface. In contrast to what we found from the integrated line flux during eclipse ingress, the line profiles during egress were fit if the receding side of the disk was brighter than the approaching edge (Figure 11). Thus the fitting routine solved the problem of the single-peaked profile by brightening the red peak at the expense of the blue peak. The problem of single-peaked profiles from accretion disks has also been encountered in the study of AGN. One possible explanation for red-shifted single-peaked lines is that gradients in the disk velocities favor the escape of photons from one side of the disk (Murray & Chiang 1997) into the line of sight.

That our model correctly matches the variation in the line profiles during both eclipse ingress (observed during the main-on state with the GHRS) and egress (observed during the short-on state with the STIS) should be considered strong confirmation of the interpretation that the broad lines arise in a disk rotating prograde with the orbit and with Keplerian velocities. This is the first determination of the rotation direction of an accretion disk in an X-ray binary. As X-ray pulsars, including Her X-1, are known to change the sign of their spin period derivative (Nelson et al. 1997), it has been speculated that counter-rotating accretion disks are possible. That the broad line flux was 50% greater during the main-on state suggests that the disk is more highly inclined to the line of sight during the short-on state, as expected, but more observations are required to separate the 35-day phase variability from random fluctuations.

If we calculate from this model the eclipse ingress light curve, the result does not fit the observations. We offer two possible explanations for the inconsistency between the eclipse ingress light curve, which suggests a symmetric disk, and the eclipse egress line profiles, which do not. One is that during the interval of ≈ 2 days between the ingress and egress, the disk precessed enough to alter the pattern of illumination and visibility on its surface.

Another possibility is that there is another source of emission in addition to the disk which is complicating the analysis. For example, the narrow lines at maximum light are ≈ 4 times brighter than the broad disk lines. For the N V lines, $A/n_e C_{21} \sim 100$, so that UV line emission from the star impinging on the disk is much more likely to be scattered than absorbed. The scattered line profiles would depend on phase, as the scattering would occur primarily from those points on the disk with a velocity of 0 along the line to the

narrow line region. (The actual velocity of the narrow line is not exactly 0, but it is less than the velocities in the disk.) The velocity of these points relative to the viewer would be 0 near $\phi = 0$ (giving rise to symmetric scattered emission on the disk) but would cause double-peaked profiles at $\phi = 0.25$ and $\phi = 0.75$ (the relative strengths of the peaks would depend on the geometry). We expect the N V line to be affected more than the other lines, as the scattered flux depends on both the strength of the narrow line flux (N V $\lambda\lambda$ 1238.8, 1242.8 is the strongest narrow line) and the optical depth of the ion in the disk (N V should have the highest optical depth, and He II λ 1640 and O V λ 1371, which are not resonance lines, should have the lowest optical depths.) We note that the red-shift of the broad N V $\lambda\lambda$ 1238.8, 1242.8 lines as determined by the Gaussian fits is greater at $\phi \approx 0.2$ than the redshift determined for the other lines. The flux of the scattered lines would depend on the projected area of the disk as seen by the star and on the local turbulence in the disk. We will discuss models of these lines in a future paper (Boroson et al. 1999).

We have suggested (Boroson et al. 1996) that the narrow line emission is due to the X-ray illuminated atmosphere of HZ Her, as this can explain the gross behavior of the line flux as a function of ϕ . In addition, the narrow line flux was approximately equal during the main-on observations observed with the GHRS (Boroson et al. 1996) and during the short-on observations reported here. The disk-formed broad lines were brighter during the main-on state.

There are two aspects of the current observations which cast doubt on whether the region that causes the narrow line emission is really the X-ray illuminated stellar atmosphere. First, the velocities of the narrow lines do not match the velocities expected from the visible, heated portion of HZ Her. This was apparent in the GHRS observations presented by Boroson et al. (1996). For the current STIS observations, we find that the narrow lines are blueshifted both at $\phi \approx 0.75$ and at $\phi \approx 0.2$.

One possibility that we have considered to explain the narrow line velocities is that there is a gas flow in the atmosphere of HZ Her tangential to the Roche surface. It has been shown that convective currents resulting from the X-ray heating of HZ Her should have velocities of only a few km s^{-1} (Dahab 1974), but ablation of a stellar atmosphere by radiation pressure has been shown to be effective by Voit (1990). Ablation of HZ Her could cause blueshifted lines at $\phi \approx 0.75$ and $\phi \approx 0.2$, but would be difficult to reconcile with the Doppler maps of optical lines (Quaintrell 1998). The optical N V line arises in a region that moves with a velocity consistent with the heated face of HZ Her. This line is formed by recombination from N VI and should thus arise in regions *hotter* than the N V λ 1240 region. Yet the optical absorption lines, which are formed in gas *cooler* than the N V λ 1240 region, also move with the expected velocity of HZ Her (Still et al. 1997, Quaintrell 1998). It does

not seem likely that the region emitting N V λ 1240 could move along the stellar surface at velocities $\sim 100 \text{ km s}^{-1}$, while sandwiched between stationary gas layers. The model does make the simple prediction, however, that the narrow lines should be red-shifted at $\phi = 0.5$.

The second problem with identifying the narrow line region with a region above HZ Her is that the narrow line flux at $\phi = 0.2$ is ≈ 0.2 of the narrow line flux at $\phi = 0.8$. The IUE observations (Figure 9) show that the *total* broad and narrow flux during our observations did not have a phase variation that was unusual compared with the historical behavior of the source. Thus it is possible that the narrow line emission at $\phi = 0.2$ is *always* ≈ 0.2 of the emission at $\phi = 0.8$.

It is possible for the continuum and narrow line to have different phase dependences, even though they both arise on HZ Her. For example, grazing incidence could enhance line emission but not continuum emission (Boyle et al. 1986), so that the lines would be brighter at the limb. The X-ray shadow of the disk on the star could then cause an orbital asymmetry that was different for the lines and continuum. We continue to suggest provisionally, in the absence of a better candidate region for the narrow lines, that they arise on HZ Her. To be consistent with the data, however, this identification needs to invoke some unknown details of the radiative transfer or the dynamics in the atmosphere to account for the line velocities and the variation of line flux with ϕ .

Her X-1 is a complex system, and difficult to unravel in detail. However, we have shown that with phase-resolved spectroscopy, we can separate two emission regions, and can examine the rotation velocities in the accretion disk. As more far UV data on this system is obtained, from our multiwavelength campaign using the HST STIS, and from the Lyman FUSE (Far-Ultraviolet Spectroscopic Explorer), we can test more detailed models that include the differences between narrow line and continuum emission, occultation and emission by the gas stream, and disk warp shapes suggested by competing theories.

Based on observations with the NASA/ESA *Hubble Space Telescope*, obtained at the Space Telescope Science Institute, which is operated by the Association of Universities for Research in Astronomy, Inc., under NASA contract GO-05874.01-94A. BB and SDV supported in part by NASA (NAG5-2532, NAGW-2685), and NSF (DGE-9350074). BB acknowledges an NRC postdoctoral associateship. HQ is employed on PPARC grant L64621.

REFERENCES

- Anderson, S.F., Wachter, S., Margon, B., Downes, R.A., Blair, W.P., & Halpern. 1994, *ApJ*, 436, 319
- Armitage, P.J., & Livio, M. 1998, *ApJ*, 493, 898
- Begelman, M.C., McKee, C.F., & Shields, G.A. 1983, *ApJ*, 271, 70
- Begelman, M.C., & McKee, C.F. 1983, *ApJ*, 271, 89
- Bohlin, R.C. 1975, *ApJ*, 200, 402
- Boroson, B. 1999, in preparation
- Boroson, B., Blair, W.P., Davidsen, A.R., Vrtilik, S.D., Raymond, J., Long, K.S., & McCray, R. 1997, *ApJ*, 491, 903
- Boroson, B., Vrtilik, S.D., McCray, R., Kallman, T., & Nagase, F. 1996, *ApJ*, 473, 1079
- Boyle, S.J., Howarth, I., Wilson, R., & Raymond, J. 1986, in *New Insights in Astrophysics: 8 Years of UV Astronomy with IUE*, ed. E.J. Rolfe (Noordwijk: ESA), 471
- Cook, J.W., Keenan, F.P., Dufton, P.L., Kingston, A.E., Pradhan, A.K., Zhang, H.L., Doyle, J.G., & Hayes, M.A. 1995, *ApJ*, 444, 936
- Crosa, L., & Boynton, P.E. 1980, *ApJ*, 235, 999
- Dahab, R.E. 1974, *ApJ*, 187, 351
- Deeter, J.E., Boynton, P.E., Miyamoto, S., Kitamoto, S., Nagase, F., & Kawai, N. 1991, *ApJ*, 383, 324
- Dubus, G., Lasota, J.-P., Hameury, J.-M., Charles, P. 1999, *MNRAS*, in press, astro-ph/9809036
- Dufton, P.L., Hibbert, A., Keenan, F.P., Kingston, A.E., & Doschek, G.A. 1985, *ApJ*, 300, 448
- Dufton, P.L., Hibbert, A., Kingston, A.E., & Doschek, G.A. 1982, *ApJ*, 257, 338
- Dupree, A.K. et al. 1978, *Nature*, 275, 400
- Gursky, H. et al. 1980, *ApJ*, 237, 163
- Howarth, I.D. & Wilson, R. 1983a, *MNRAS*, 202, 347
- Howarth, I.D., & Wilson, R. 1983b, *MNRAS*, 204, 1091
- Iping, R.C., & Petterson, J.A. 1990, *A&A*, 239, 221
- Jones, C.A., Forman, W., & Liller, W. 1973, *ApJ*, 182, L103
- Kallman, T., & McCray, R. 1982, *ApJS*, 50, 263

- Kallman, T., Boroson, B., & Vrtilik, S.D. 1998, *ApJ*, 501, 441
- Kimble, R.A., et al. 1998, *ApJ*, 492, L83
- Ko, Y.-K., and Kallman, T.R. 1994, *ApJ*, 431, 273
- Kondo, Y., Wolff, C.L., & van Flandern, T.C. 1983, *ApJ*, 273, 716
- Kong, A.K.H., Charles, P.A., & Kuulkers, E. 1998, *NewA*, 3, 301
- Lai, D. 1999, *ApJ* submitted, astro-ph/9904110
- Levine, A.M., Bradt, H., Wei, C., Jernigan, J.G., Morgan, E.H., Remillard, R., Shirey, R.E., Smith, D.A. 1996, *ApJ*, 469, L33
- Lubow, S.H., & Shu, F.H. 1975, *ApJ*, 198, 383
- Maloney, P.R., & Begelman, M.C. 1997, *ApJ*, 491, L43
- Maloney, P.R., Begelman, M.C., & Pringle, J.E. 1996, *ApJ*, 472, 582
- Mavromatakis, F. 1993, *A&A*, 273, 147
- Murray, N., & Chiang, J. 1997, *ApJ*, 474, 91
- Nelson, R. et al. 1997, *ApJ*, 488, L117
- Press, W.H., Teukolsky, S.A., Vetterling, W.T., & Flannery, B.P. 1992, *Numerical Recipes: The Art of Scientific Computing* (New York: Cambridge University Press)
- Pringle, J.E. 1996, *MNRAS*, 281, 357
- Pringle, J.E. 1997, *MNRAS*, 292, 136
- Quaintrell, H. 1998, Ph.D. Thesis
- Raymond, J. 1993, *ApJ*, 412, 267
- Schandl, S. 1996, *A&A*, 307, 95
- Schandl, S., & Meyer, F. 1994, *A&A*, 289, 149
- Schwarzenberg-Czerny, A. 1992, *A&A*, 260, 268
- Scott, D.M. & Leahy, D.A. 1999, *ApJ*, 510, 974
- Shakura, N.I., et al. 1998, *MNRAS*, 300, 992
- Shakura, N.I., & Sunyaev, R.A. 1973, *A&A*, 24, 337
- Smak, J. 1981, *Acta Astron.* 31, 395
- Still, M.D., Quaintrell, H., Roche, P.D., & Reynolds, A.P. 1997, *MNRAS*, 292, 52
- Trümper, J., Kahabka, P., Ögelman, H., Pietsch, W., & Voges, W. 1986, *ApJ*, 300, L63

- van Paradijs, J., & McClintock, J.E. 1995, in *X-ray Binaries*, ed. W.H.G. Lewin, J. van Paradijs, & E.P.J. van den Heuvel (Cambridge: Cambridge University Press), 59
- Verner, D.A., Barthel, P.D., & Tytler, D. 1994, *A&AS*, 108, 287
- Voit, G.M. 1990, Ph.D. thesis
- Vrtilek, S.D., et al. 1999, in preparation
- Vrtilek, S.D, & Halpern, J.P. 1985, *ApJ*, 296, 606
- Vrtilek, S.D., Cheng, F.H., & Raymond, J. 1996, *ApJ*, 465, 915
- Vrtilek, S.D., Raymond, J.C., Garcia, M.R, Verbunt, F., Hasinger, G., & Kurster, M. 1990, *A&A*, 235, 165
- Wijnands, R.A.D., Kuulkers, E., & Smale, A.P. 1996, *ApJ*, 473, 45
- Woodgate, B.E. et al. 1998, *PASP*, 110, 1183

Fig. 1.— The UV spectrum of Her X-1 observed with the HST STIS in echelle mode, averaged over $\phi = 0.685 - 0.764$.

Fig. 2.— Gaussian fits to the N V $\lambda\lambda 1238.8, 1242.8$ doublet as observed with the HST STIS in echelle mode during July, 1998. The broad and narrow line fits are shown separately.

Fig. 3.— Gaussian fits to the O V $\lambda 1371$ line as observed with the HST STIS in July, 1998. We show only the total of the broad and narrow line fits.

Fig. 4.— Gaussian fits to the Si IV $\lambda 1393$ line as observed with the HST STIS in July, 1998.

Fig. 5.— Gaussian fits to the C IV $\lambda\lambda 1548.195, 1550.77$ doublet as observed with the HST STIS in July, 1998.

Fig. 6.— Gaussian fits to the He II $\lambda 1640.47$ line as observed with the HST STIS in July, 1998.

Fig. 7.— Velocities of broad (* symbols) and narrow (+ signs) lines from Gaussian fits, versus orbital phase. The expected velocities of the neutron star, the center of mass of HZ Her, and the L1 Lagrangian point are indicated.

Fig. 8.— Orbital phase variations in the fluxes of broad and narrow N V line components from STIS observations.

Fig. 9.— Flux of the N V $\lambda 1240$ line, the C IV line, and the continuum (1260Å to 1630Å) as observed with IUE, versus orbital phase. The diamonds show the fluxes observed with the HST STIS.

Fig. 10.— A test of the left-right symmetry of the disk. The x axis shows the expected position of the eclipse line of HZ Her on the disk, relative to the neutron star. The * points mark disk fluxes observed, while the + points mark the amount of disk flux occulted, reflected about $x = 0$. We show flux in (a) the N V lines, (b) the C IV lines, (c) the continuum (1260Å to 1630Å).

Fig. 11.— Model fits to the N V emission lines. Upper panels: observed and best-fit (bold) fluxes for the July 1998 observations. Lower panels: observed and best-fit fluxes for the GHRSS observations of August 1994 (Boroson et al. 1996). Lower right panel: the best-fit empirical distribution of flux with angle on the disk.

Fig. 12.— Emission lines in the 1400Å region which can serve as density diagnostics. The vertical dashed lines indicate the rest wavelength of the lines. The spectrum has been redshifted to account for a blue-shift of $\approx 50 \text{ km s}^{-1}$ in all of the lines.

Fig. 13.— The density versus temperature in the narrow line emission region implied by different line ratios

Fig. 14.— Narrow absorption lines blueshifted at 500km s^{-1} . The vertical dashed lines mark -500km s^{-1} heliocentric velocity in each of the doublet components. In panels (a) through (e) respectively, we show the spectrum at $\phi = 0.057, 0.092, 0.132, 0.171, 0.211$. In the right-hand panels, we show the differences of the spectra from the spectrum at $\phi = 0.057$.

Table 1. The STIS observation log

Root name	STIS mode ^a	Start (MJD)	Exposure (s)	Orbital Phase ^b
O4V401010	L	51004.563157	565	0.906
O4V401020	L	51004.571792	1517	0.917
O4V401030	L	51004.623308	1495	0.947
O4V401040	L	51004.646178	1702	0.962
O4V401050	L	51004.702278	444	0.987
O4V403010	E	51006.513968	2227	0.057
O4V403020	E	51006.571780	2636	0.092
O4V403030	E	51006.638968	2636	0.132
O4V403040	E	51006.706155	2636	0.171
O4V403050	E	51006.773342	2620	0.211
O4V404010	E	51007.522127	2227	0.650
O4V404020	E	51007.579581	2636	0.685
O4V404030	E	51007.646768	2636	0.725
O4V404040	E	51007.713968	2636	0.764
O4V404050	E	51007.781155	2620	0.804

^a‘L’ denotes low-resolution observations, and ‘E’ denotes echelle observations

^bThe orbital phase of the mid-exposure time, using the ephemeris of Deeter et al. (1991)

Table 2. Gaussian fits to the UV lines

ϕ	V_n^a	ΔV_n^b	F_n^c	V_{broad}	ΔV_b	F_b	χ_ν^2, ν
Line:				N V			
0.057				-391 ± 371	160 ± 279	0.40 ± 0.24	2.45, 238
0.092				-38 ± 24	832 ± 66	4.12 ± 0.23	5.95, 238
0.132				-15 ± 6	854 ± 12	4.77 ± 0.06	7.40, 238
0.171	-168 ± 188	66 ± 18	0.25 ± 0.06	7 ± 28	822 ± 18	4.66 ± 0.10	7.32, 234
0.211	-126 ± 139	65 ± 36	0.44 ± 0.12	26 ± 17	831 ± 36	4.99 ± 0.17	7.35, 234
0.650	-51 ± 2	182 ± 84	6.77 ± 0.31	207 ± 41	569 ± 84	4.88 ± 0.51	17.67, 234
0.685	-67 ± 1	154 ± 127	5.43 ± 0.17	211 ± 29	654 ± 127	5.96 ± 0.45	18.82, 234
0.725	-73 ± 36	140 ± 82	4.04 ± 0.17	228 ± 32	656 ± 82	5.85 ± 0.62	14.36, 234
0.764	-94 ± 1	151 ± 75	3.75 ± 0.12	224 ± 32	702 ± 75	5.01 ± 0.35	10.1, 234
0.804	-104 ± 112	154 ± 127	2.66 ± 0.20	217 ± 66	866 ± 127	5.52 ± 0.51	12.21, 234
Line:				Si IV			
0.057				-453 ± 16	298 ± 37	0.16 ± 0.01	0.42, 141
0.092				-226 ± 69	940 ± 267	0.72 ± 0.47	2.7, 141
0.132				-202 ± 50	889 ± 181	0.86 ± 0.38	3.8, 141
0.171	-87 ± 8	23 ± 42	0.02 ± 0.01	-151 ± 13	893 ± 42	0.88 ± 0.05	4.17, 137
0.211	-129 ± 4	68 ± 285	0.04 ± 0.01	-161 ± 17	937 ± 285	0.63 ± 0.21	5.20, 137
0.650	-49 ± 3	180 ± 6	0.71 ± 0.02	124 ± 14	415 ± 6	0.36 ± 0.03	12.72, 137
0.685	-78 ± 2	145 ± 30	0.59 ± 0.01	266 ± 13	446 ± 30	0.33 ± 0.02	6.47, 137
0.725	-111 ± 6	152 ± 29	0.24 ± 0.05	131 ± 43	541 ± 29	0.31 ± 0.04	8.44, 137
0.764	-127 ± 2	72 ± 24	0.16 ± 0.01	101 ± 16	618 ± 24	0.46 ± 0.02	6.1, 137
0.804	-113 ± 7	286 ± 14	0.44 ± 0.02	310 ± 23	517 ± 14	0.33 ± 0.03	4.06, 137

Table 2—Continued

ϕ	V_n^a	ΔV_n^b	F_n^c	V_{broad}	ΔV_b	F_b	χ_ν^2, ν
Line:				O V			
0.057				-429 ± 119	628 ± 488	0.08 ± 0.10	0.38, 218
0.092				15 ± 145	580 ± 510	0.30 ± 0.52	2.64, 218
0.132	213 ± 6	214 ± 48	0.17 ± 0.01	-667 ± 22	773 ± 48	0.35 ± 0.02	3.81, 214
0.171	164 ± 8	284 ± 104	0.23 ± 0.01	-631 ± 46	393 ± 104	0.13 ± 0.02	3.56, 214
0.211	-174 ± 24	6 ± 0	0.0 ± 0.01	-52 ± 4	130 ± 0	0.14 ± 0.01	5.33, 214
0.650	-80 ± 4	263 ± 10	0.94 ± 0.05	335 ± 36	570 ± 10	0.43 ± 0.02	7.47, 214
0.685	-81 ± 1	216 ± 3	1.01 ± 0.01	351 ± 10	447 ± 3	0.43 ± 0.02	8.27, 214
0.725	-77 ± 1	168 ± 6	0.63 ± 0.01	343 ± 7	383 ± 6	0.48 ± 0.02	7.62, 214
0.764	-79 ± 2	210 ± 21	0.51 ± 0.05	380 ± 54	433 ± 21	0.30 ± 0.08	5.68, 214
0.804	-122 ± 4	369 ± 9	0.60 ± 0.01	495 ± 11	427 ± 9	0.31 ± 0.02	4.50, 214
Line:				C IV			
0.057				-400 ± 11	322 ± 38	0.74 ± 0.09	0.68, 234
0.092				-120 ± 19	789 ± 33	2.65 ± 0.54	1.46, 234
0.132				-146 ± 25	742 ± 38	3.34 ± 0.58	2.71, 234
0.171	-160 ± 26	54 ± 86	0.25 ± 0.15	-115 ± 30	929 ± 86	3.98 ± 0.62	2.90, 230
0.211	-129 ± 13	66 ± 69	0.44 ± 0.22	-186 ± 13	915 ± 69	5.7 ± 1.1	3.28, 230
0.650	-56 ± 2	222 ± 88	3.93 ± 0.47	194 ± 36	536 ± 88	2.30 ± 0.45	5.38, 230
0.685	-73 ± 2	190 ± 84	2.68 ± 0.44	182 ± 29	602 ± 84	4.65 ± 1.09	4.33, 230
0.725	-86 ± 4	129 ± 63	1.29 ± 0.22	251 ± 22	655 ± 63	3.99 ± 0.37	4.64, 230
0.764	-116 ± 8	93 ± 57	0.94 ± 0.22	121 ± 23	611 ± 57	7.41 ± 1.69	4.83, 230
0.804	-131 ± 7	108 ± 38	0.81 ± 0.21	93 ± 27	589 ± 38	3.26 ± 0.47	3.54, 230

Table 2—Continued

ϕ	V_n^a	ΔV_n^b	F_n^c	V_{broad}	ΔV_b	F_b	χ_ν^2, ν
Line:				He II			
0.057				-282 ± 44	412 ± 140	0.26 ± 0.08	0.26, 163
0.092				-141 ± 27	699 ± 120	0.83 ± 0.17	1.1, 163
0.132				-78 ± 29	605 ± 78	0.76 ± 0.13	1.43000, 163
0.171				-112 ± 16	640 ± 33	0.95 ± 0.06	1.30, 159
0.211	-58 ± 7	143 ± 63	0.24 ± 0.04	-110 ± 26	642 ± 63	0.86 ± 0.07	2.01, 159
0.650	-67 ± 9	220 ± 27	1.45 ± 0.18	203 ± 49	674 ± 27	0.91 ± 0.15	3.75, 159
0.685	-82 ± 1	185 ± 5	1.11 ± 0.02	109 ± 12	620 ± 5	1.22 ± 0.09	3.60, 159
0.725	-94 ± 4	162 ± 13	0.75 ± 0.05	108 ± 17	682 ± 13	1.28 ± 0.07	2.89, 159
0.764	-89 ± 3	165 ± 13	0.65 ± 0.05	6 ± 26	955 ± 13	1.75 ± 0.15	2.82, 159
0.804	-106 ± 5	161 ± 22	0.47 ± 0.07	35 ± 21	705 ± 22	1.09 ± 0.09	2.26, 159

^aHeliocentric velocity of the narrow line component in km s^{-1}

^bFull Width Half Maximum of fit to the narrow line component in km s^{-1}

^cFlux in the narrow line, in $10^{-13} \text{ erg s}^{-1} \text{ cm}^{-2}$. For the doublets, we give the total flux in both doublet components.

Phase	F_{1238}/F_{1242} (broad)	F_{1238}/F_{1242} (narrow)
0.057	1.10 ± 0.20	
0.092	1.34 ± 0.17	
0.132	1.46 ± 0.03	
0.171	1.54 ± 0.06	1.44 ± 0.35
0.192	1.58 ± 0.08	1.40 ± 0.30
0.211	0.94 ± 0.11	1.28 ± 0.06
0.650	1.16 ± 0.10	1.23 ± 0.23
0.685	1.17 ± 0.10	1.24 ± 0.11
0.725	1.11 ± 0.09	1.27 ± 0.05
0.804	1.18 ± 0.08	1.30 ± 0.08

Table 3: Doublet ratios for the N V λ 1238.821, 1242.804 lines from Gaussian fits to the broad and narrow components.

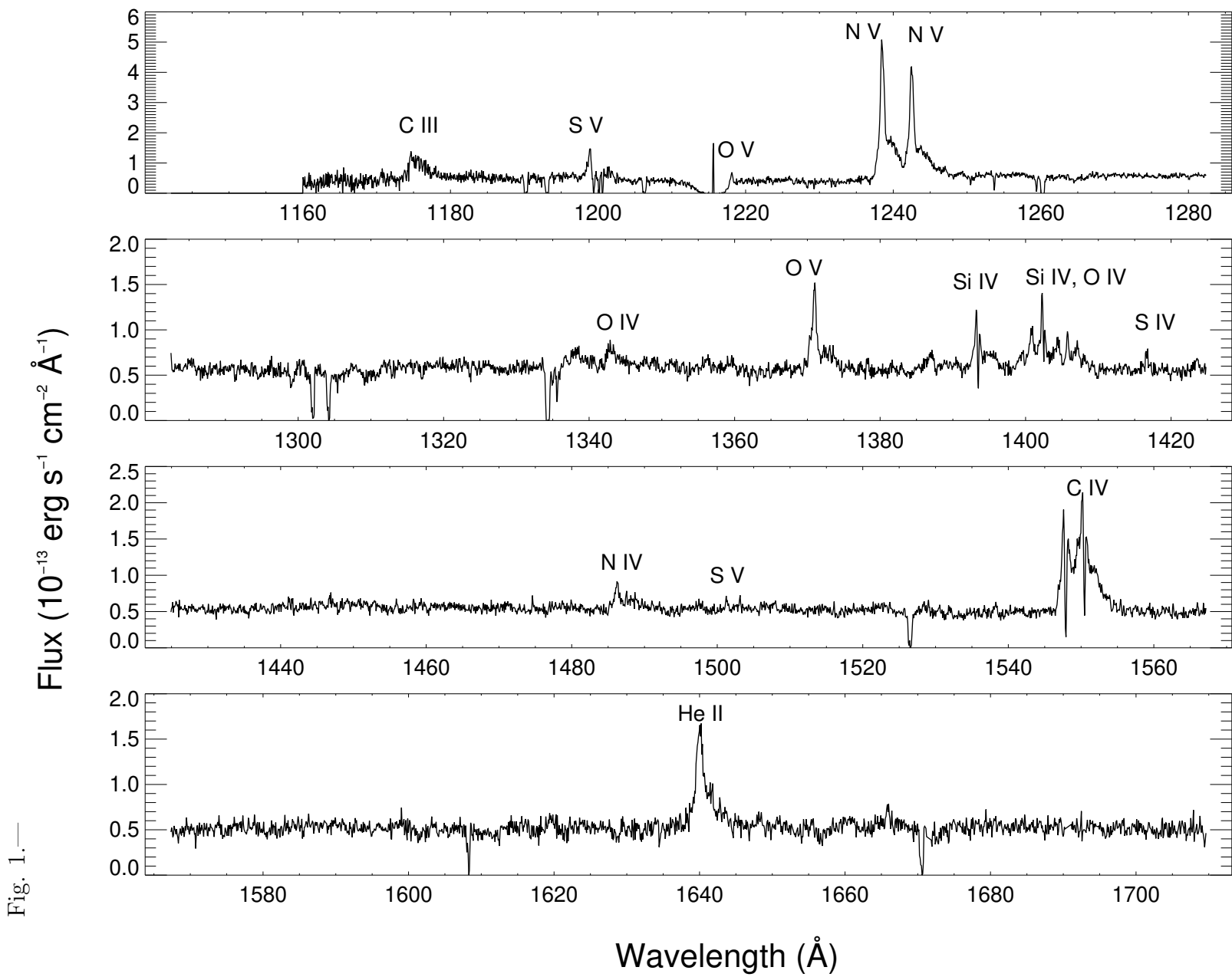


Fig. 1.—

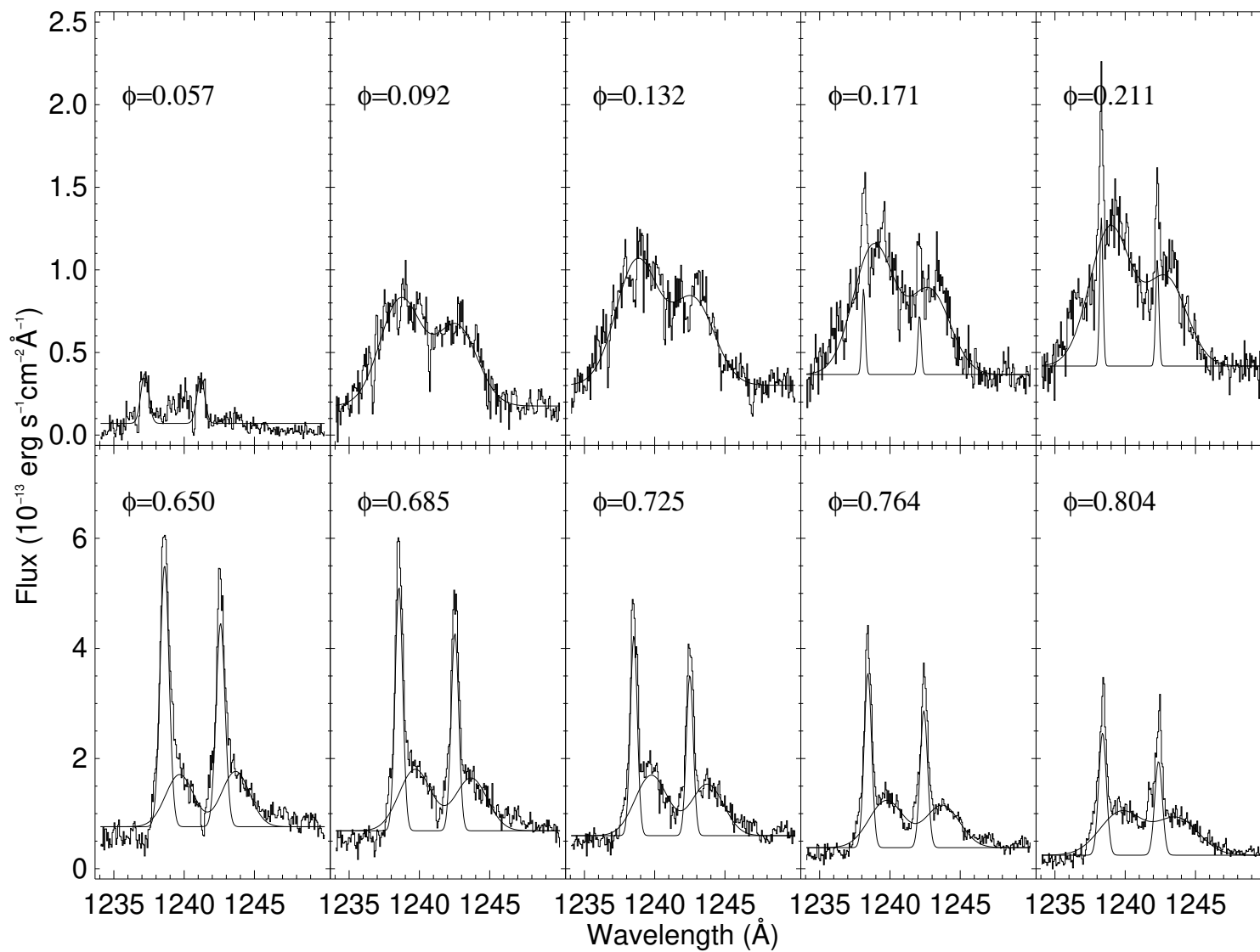


Fig. 2.—

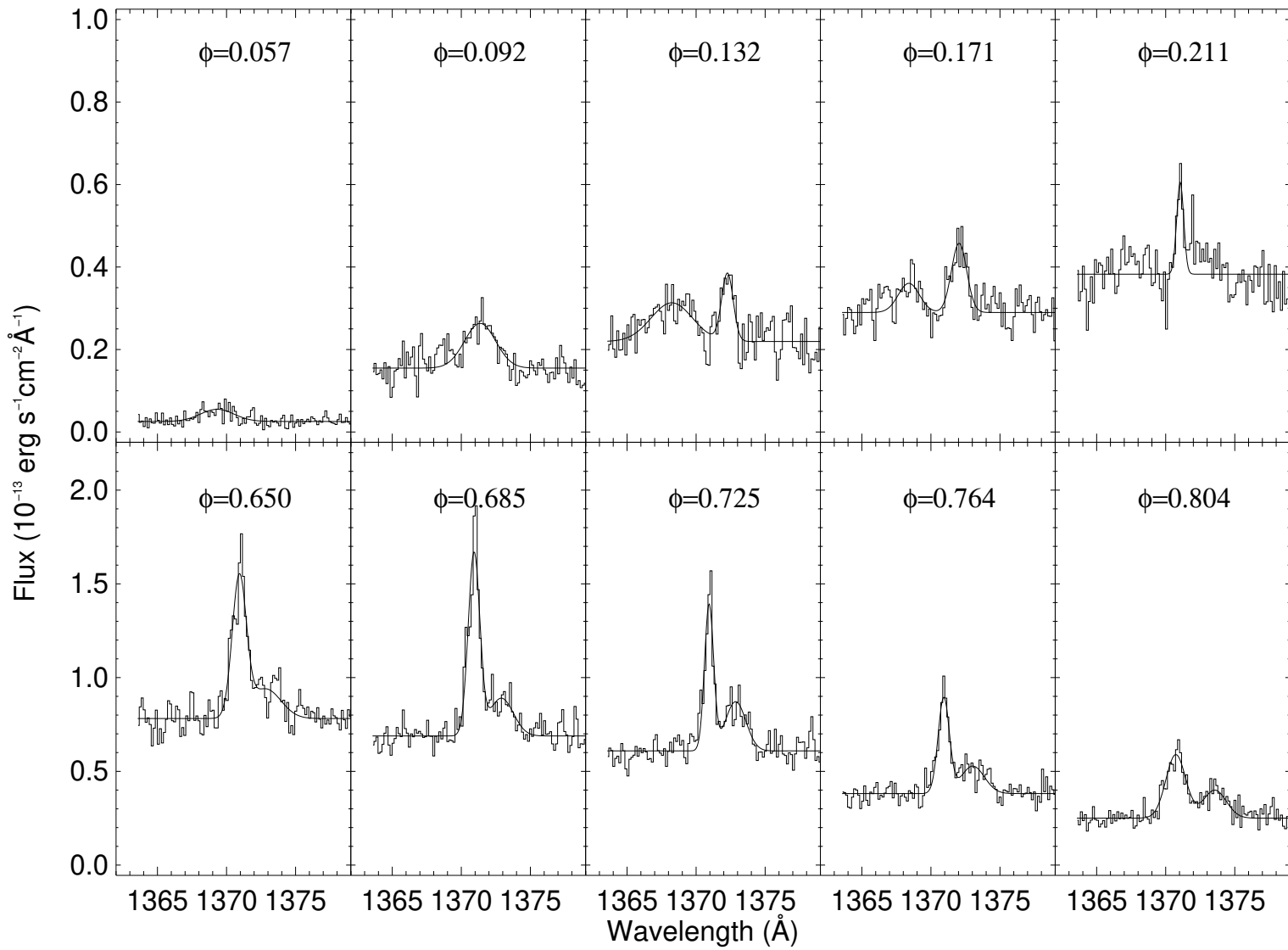


Fig. 3.—

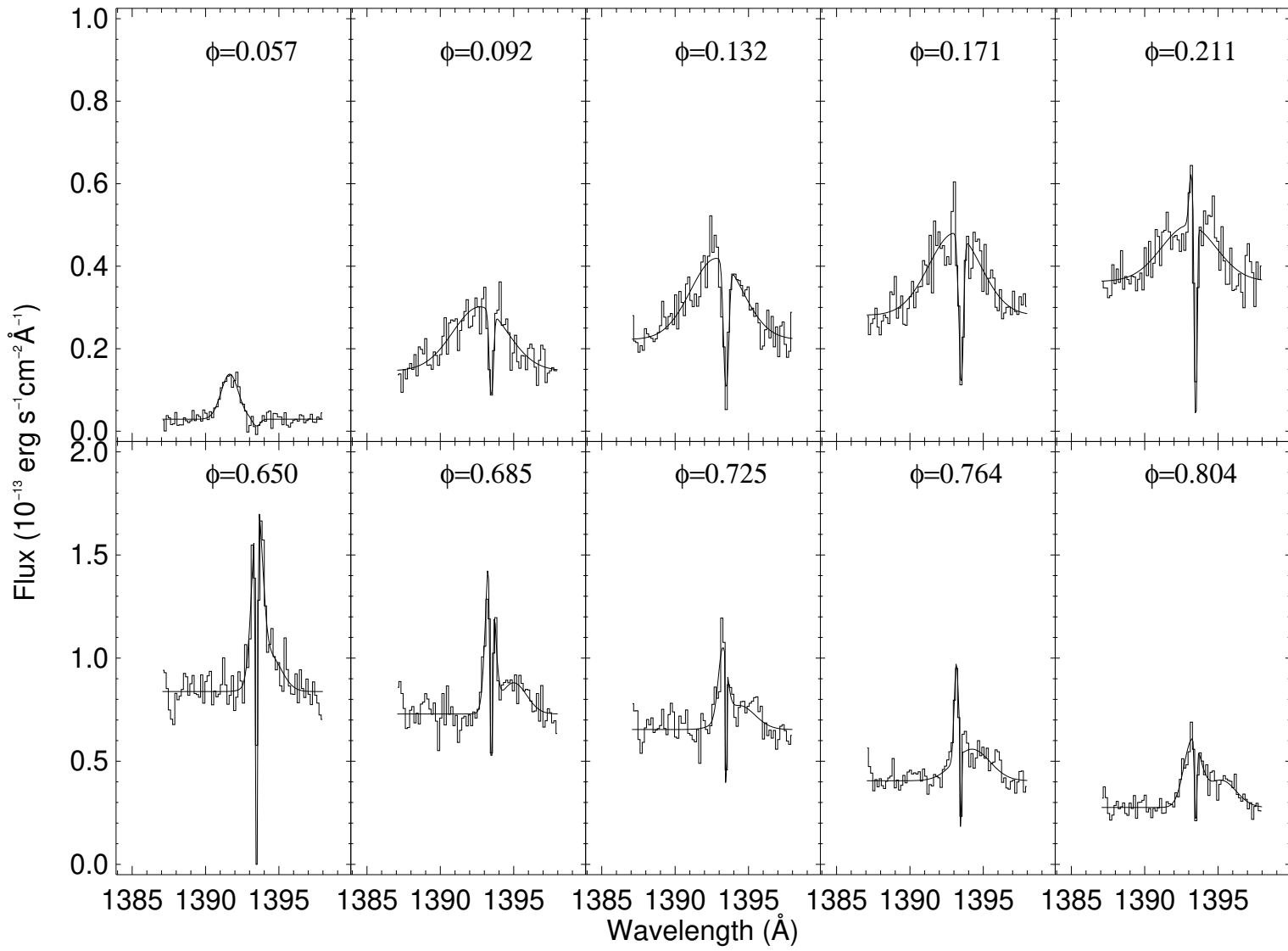


Fig. 4.—

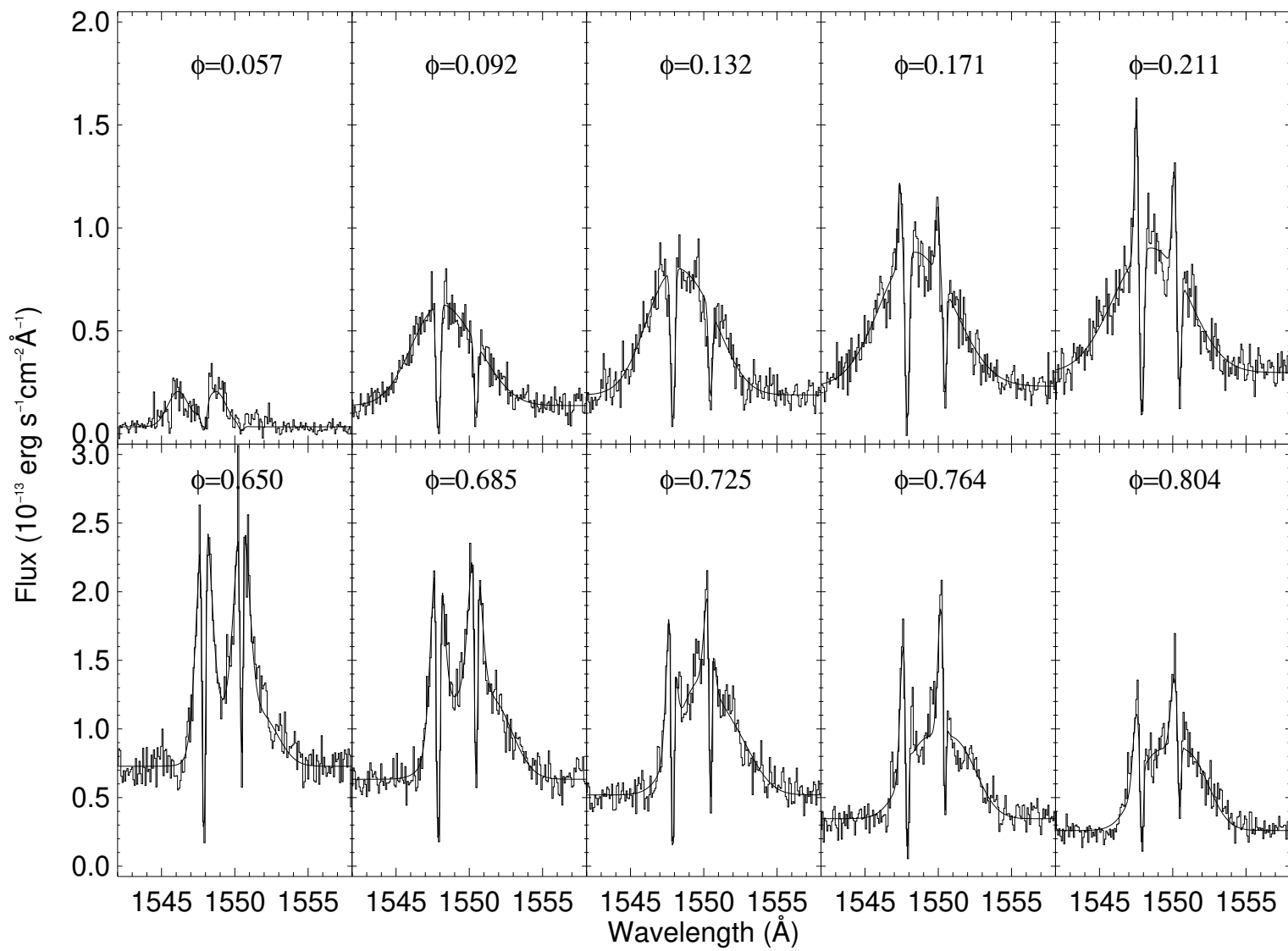


Fig. 5.—

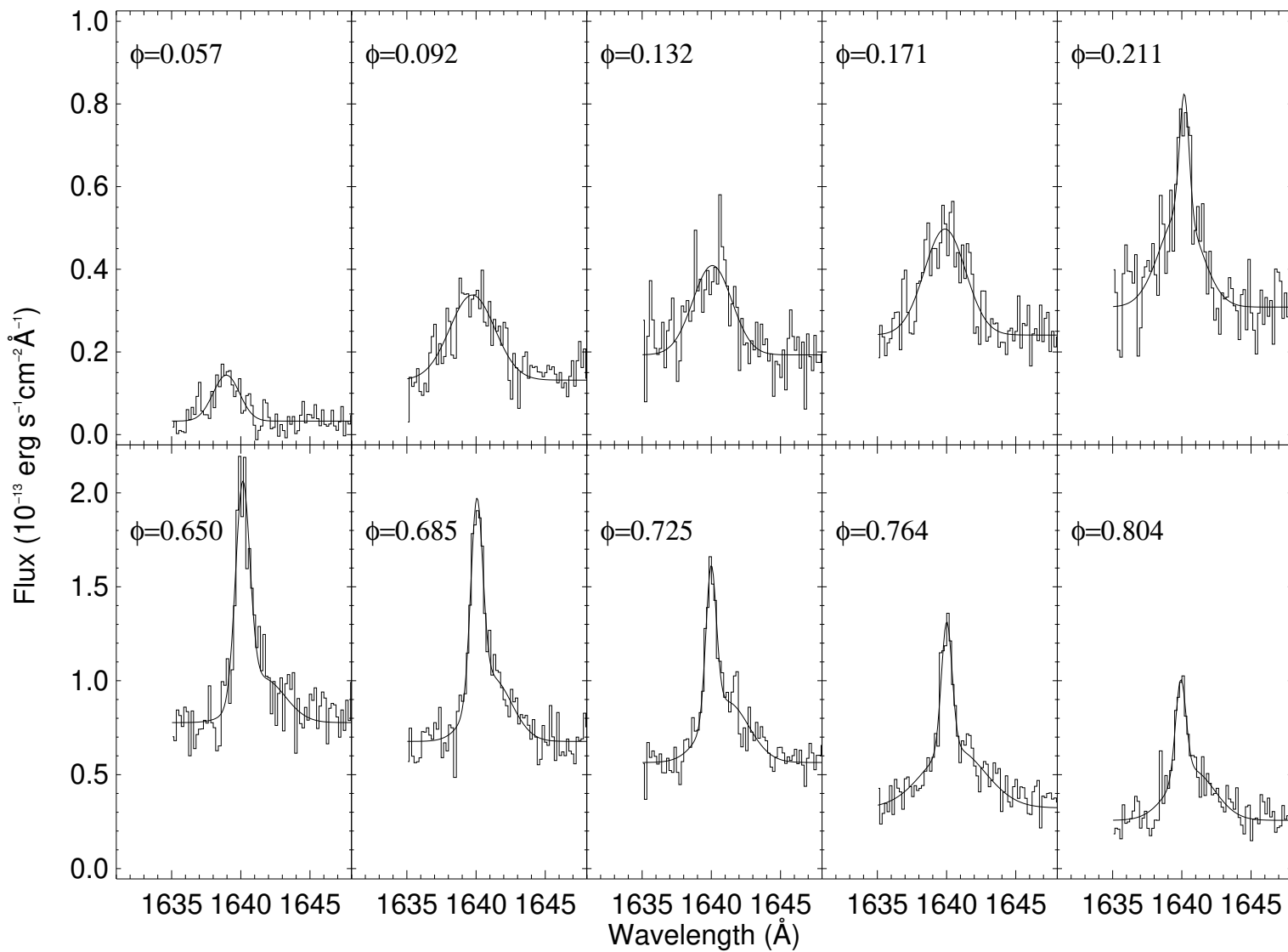


Fig. 6.—

Fig. 7.—

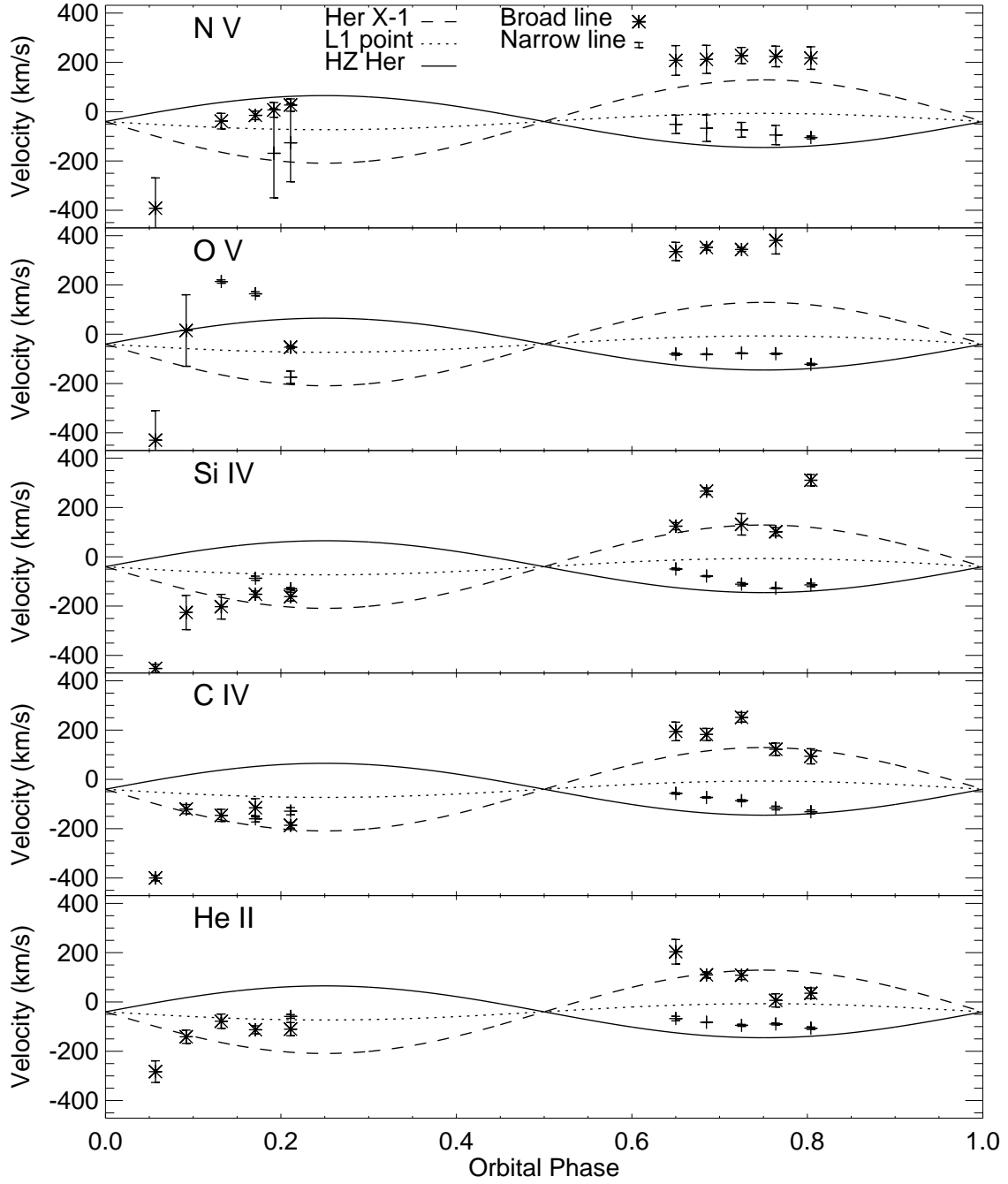


Fig. 8.—

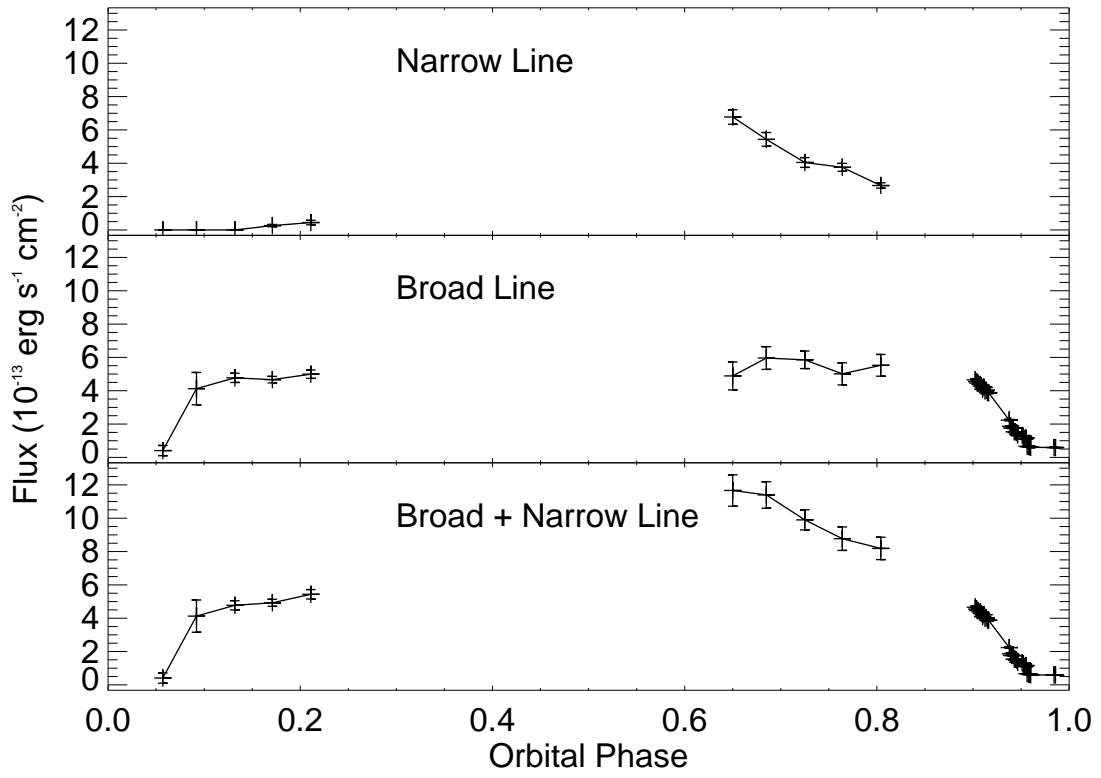


Fig. 9.—

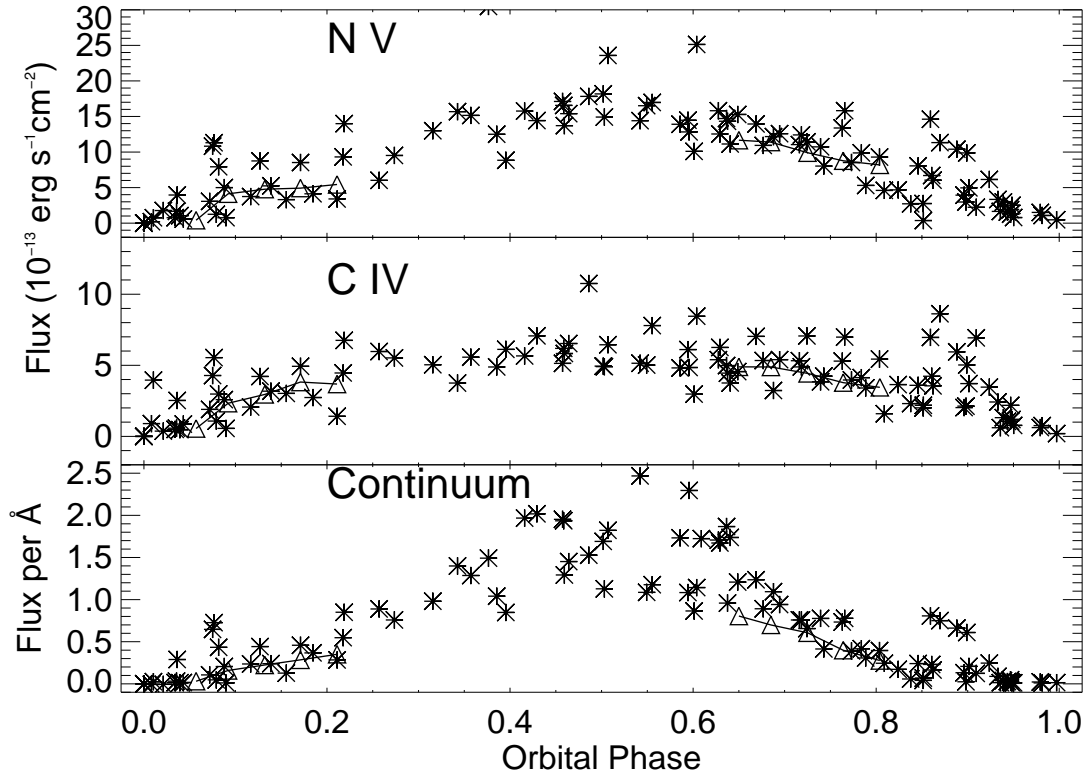


Fig. 10.—

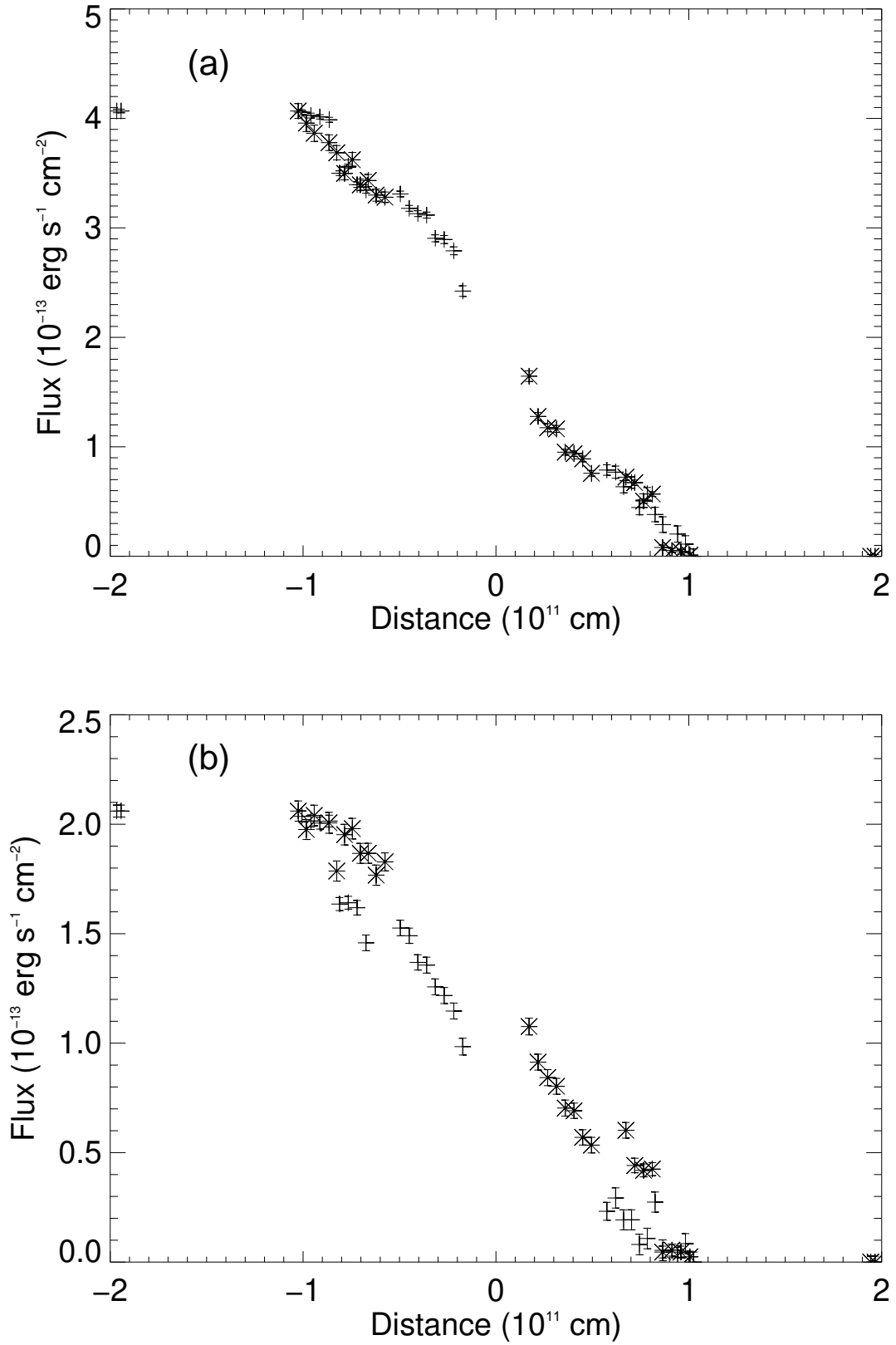
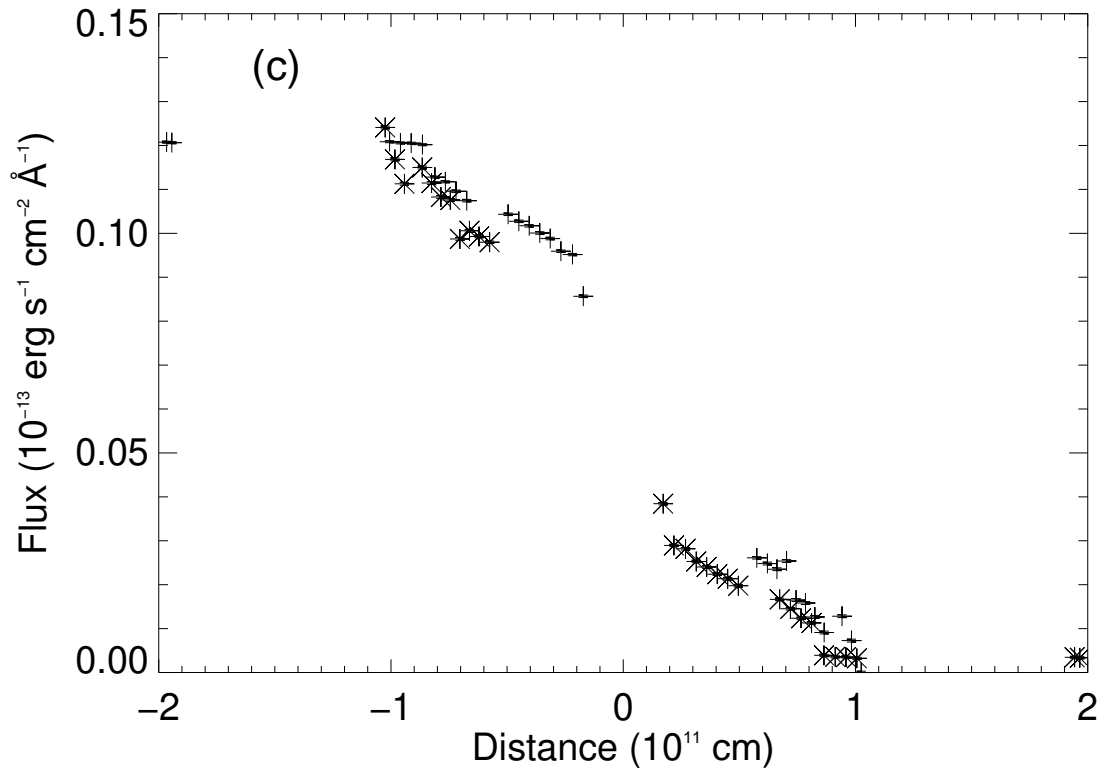


Fig. 10.—



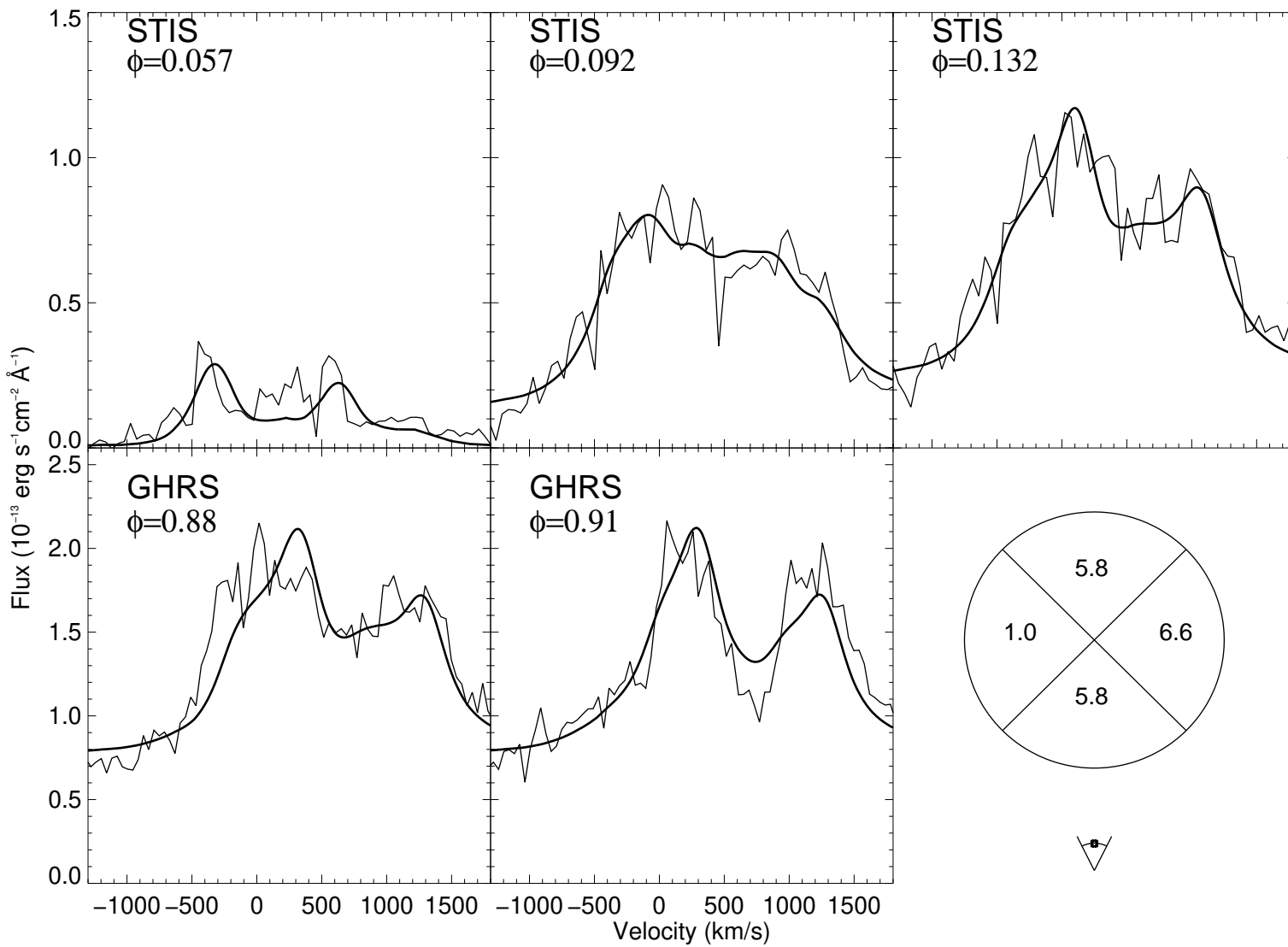


Fig. 11.—

Fig. 12.—

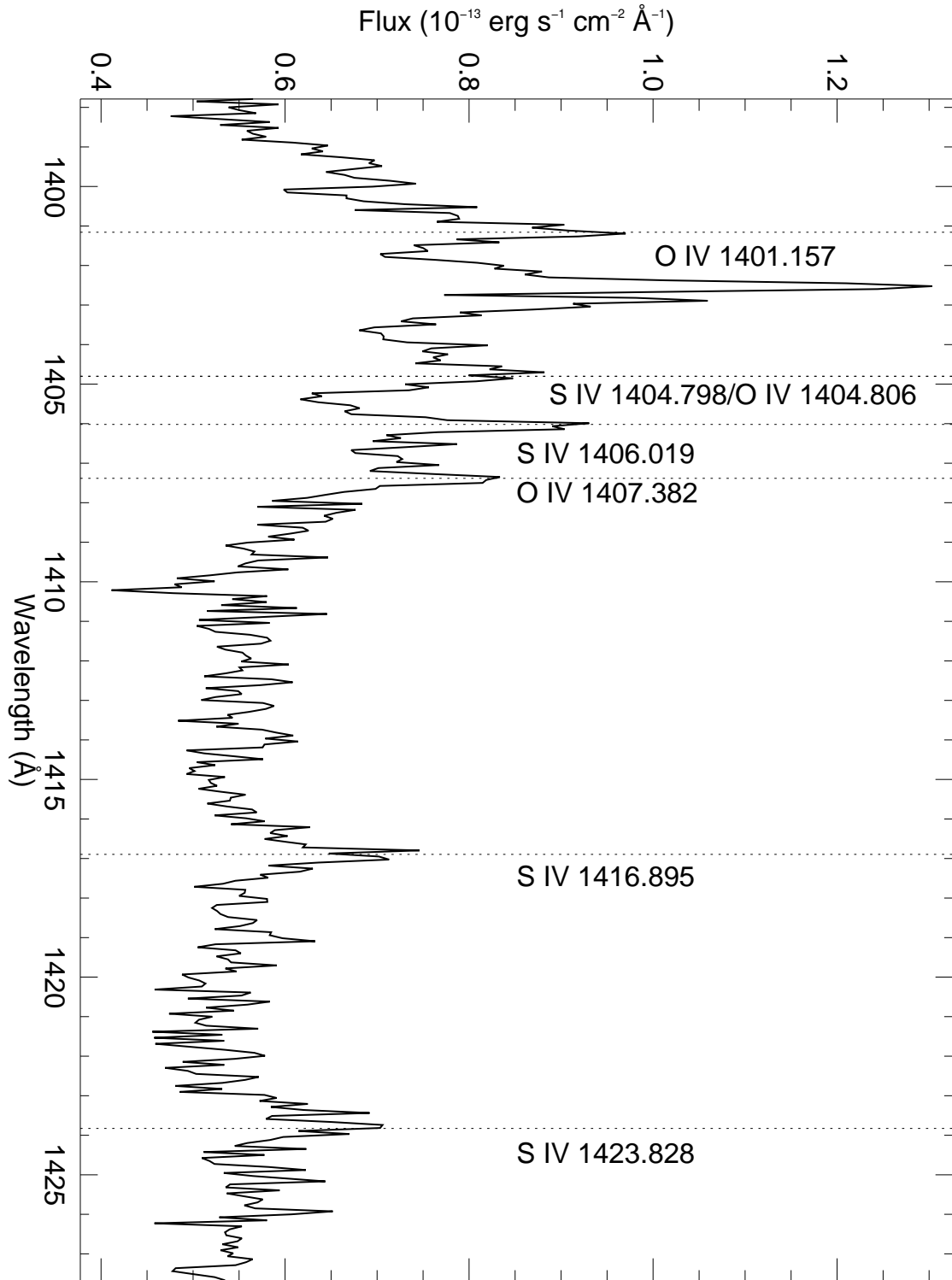


Fig. 13.—

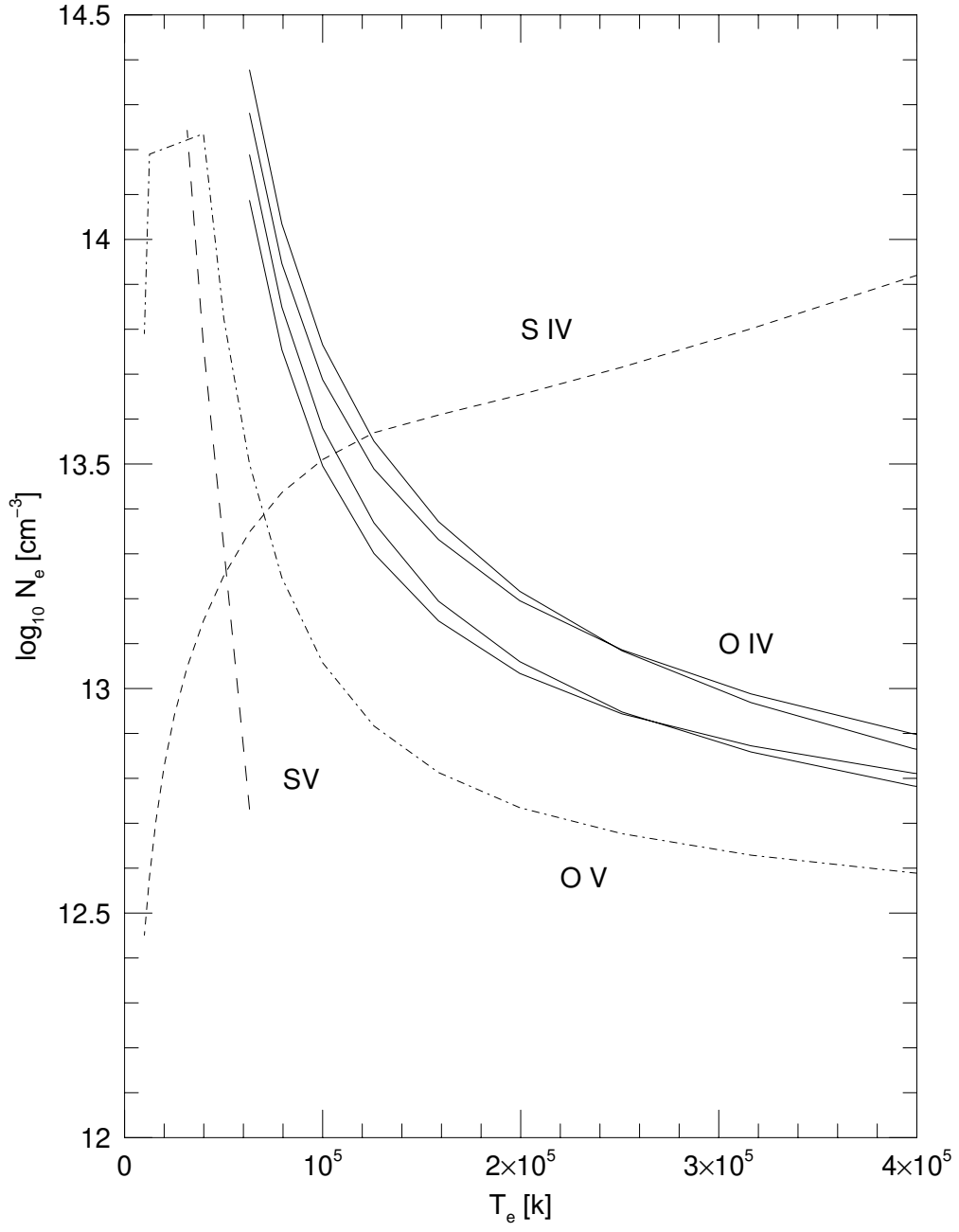


Fig. 14.—

